

Flares and magnetic non-potentiality of NOAA AR 11158 *

Qiao Song¹, Jun Zhang¹, Shu-Hong Yang¹ and Yang Liu²

¹ Key Laboratory of Solar Activity, National Astronomical Observatories, Chinese Academy of Sciences, Beijing 100012, China; qsong@nao.cas.cn; zjun@nao.cas.cn; shuhongyang@nao.cas.cn

² W. W. Hansen Experimental Physics Laboratory, Stanford University, Stanford, CA 94305-4085, USA; yliu@sun.stanford.edu

Received 2012 July 16; accepted 2012 September 20

Abstract Magnetic non-potentiality is important for understanding flares and other solar activities in active regions (ARs). Five non-potential parameters, i.e. electric current, current helicity, source field, photospheric free energy, and angular shear, are calculated to quantify the non-potentiality of NOAA AR 11158. Benefitting from the high spatial resolution, high cadence and continuous temporal coverage of vector magnetograms from the Helioseismic and Magnetic Imager onboard the *Solar Dynamics Observatory*, both the long-term evolution of the AR and the rapid change during flares are studied. We confirm that, compared with the magnetic flux, the magnetic non-potentiality has a closer connection with the flare, and the emerging flux regions are important for understanding the magnetic non-potentiality and flares. The main results are as follows. (1) The vortex in the source field directly displays the deflection of the horizontal magnetic field. The deflection corresponds to the fast rotating sunspot with a time delay, which suggests that the sunspot rotation leads to an increase in the non-potentiality. (2) Two areas that have evident changes in the azimuth of the vector magnetic field are found near the magnetic polarity inversion line. The change rates of the azimuth are about 1.3° h^{-1} and 3.6° h^{-1} , respectively. (3) Rapid and prominent increases are found in the variation of helicity during four flares in the regions where their initial brightening occurs. The recovery of the increases takes 3–4 h for the two biggest flares (X2.2 and M6.6), but only takes about 2 h for the two other smaller flares (M2.2 and M1.6).

Key words: Sun: activity — Sun: flares — Sun: magnetic fields — Sun: photosphere — sunspots

1 INTRODUCTION

Solar flares, a common but powerful active phenomenon in the Sun which can release up to the order of 10^{32} erg energy (Kopp et al. 2005), have received much attention over the past two centuries. It is generally believed that the enormous energy from a solar flare is provided by the magnetic field. When the magnetic field of a solar active region (AR) deviates from a potential (current-free) field

* Supported by the National Natural Science Foundation of China.

configuration to a non-potential configuration, i.e. becomes more sheared and/or twisted, the energy will be stored in the stressed magnetic field and finally it will be released by flares, eruptive filaments, and coronal mass ejections (CMEs) (Gary et al. 1987; Sakurai 1989; Schrijver et al. 2008; Sun et al. 2012). The deviation of an observed vector magnetic field from the potential magnetic configuration is referred to as the magnetic non-potentiality.

Non-potential parameters were introduced to measure the magnetic non-potentiality of ARs. The electric current density is directly calculated from the curl of a vector magnetic field. Due to a lack of accurate observations of the magnetic field in the higher layers of the solar atmosphere, the vertical component of electric current density (J_z) in the photosphere is widely used (Wang 1999; Moon et al. 2000). In a practical calculation, the pixels of a vector magnetogram with low signal-to-noise (S/N) ratios often have unreasonably strong currents. The electric current helicity can avoid this problem by increasing the effect of magnetic field strength on the current. As a scalar, the helicity of vertical current (h_c) is also called the fractional current helicity (Abramenko et al. 1996; Bao & Zhang 1998). The angular shear and two other non-potential parameters come from the differences between the observed magnetic field and the potential magnetic field which is extrapolated from the observed photospheric field with assumptions about the potential field. Hagyard et al. (1984) defined the angular magnetic shear as the angular degree difference between the observed horizontal field and the horizontal component of the potential field. Lu et al. (1993) pointed out that the shear angle, which is defined by the angle between the vector of an observed magnetic field and the vector of a computed potential field, is a better indicator for the twisting effect of the vector magnetic field. Wang et al. (1996) defined a sign on the shear angle to introduce the angular shear (θ_{as}). The sign is determined by the direction of rotation from the horizontal component of the potential field vector compared to the horizontal component of the observed magnetic field vector with a clockwise rotation considered as negative. Since the angular shear only needs the angles of vectors, it does not encounter errors caused by the calibration of magnetic field strength. Hagyard et al. (1981) defined the source field (\mathbf{B}_s) as the vector departure. The source field is a comprehensive, vectorial expression of magnetic non-potentiality which is given by $\mathbf{B}_s = \mathbf{B}_{obs} - \mathbf{B}_{pot}$, where the subscripts 'obs' and 'pot' refer to the observed and potential magnetic field respectively. The photospheric free energy density (ρ_{free}) is proportional to the square of the strength of the source field.

Through the parameters, the relationship between flares and the non-potentiality has been studied. Schrijver et al. (2005) sampled 95 ARs and concluded that flares are 2.4 times more frequent in non-potential ARs than in potential ARs. Some studies on the spatial relationship showed that initial bright kernels of flares are located in the vicinities of peaks of some non-potential parameters (Hagyard et al. 1984; Wang et al. 1994b). An increase of magnetic shear was found after several X-class flares (Wang et al. 1994a, 2002). Deng et al. (2001) demonstrated that the magnetic shear changed its sign in the filament channel of NOAA AR 9077. Rapid and irreversible increases in the horizontal magnetic field (B_h) during flares were also found (Wang et al. 2009, 2012; Liu et al. 2012; Sun et al. 2012) in the areas around the magnetic polarity inversion line (PIL). Furthermore, it has been shown that the emergence of magnetic flux plays an important role in the development of the non-potentiality and eventually produces flares/CMEs. New emerging bipoles were found to be cospatial with significant vertical electric currents (Wang et al. 1994b; Leka et al. 1996). Wang et al. (2004) further noted that some emerging flux regions (EFRs) brought an opposite sign to the dominant helicity and the initiation site of the flare/CME, which was characterized by the opposite sign and magnetic flux cancelation. Other studies also showed the emergence of twisted magnetic flux ropes and the injection of opposite helicity involved with strong X-class flares (Dun et al. 2007; Park et al. 2010).

It is well known that vector magnetic field observation is irreplaceable for the study of non-potentiality. The Helioseismic and Magnetic Imager (HMI; Schou et al. 2012) onboard the *Solar Dynamics Observatory* (SDO; Pesnell et al. 2012) provides uninterrupted high cadence and high spatial resolution full-disk vector magnetic field observation without atmospheric distortion. This

unprecedented observing ability allows us to simultaneously investigate the evolution of an AR over a long period and monitor the short-term changes in the non-potentiality during flares of the AR. In order to achieve this goal, we focus on temporal and spatial variations of the photospheric magnetic field in detail. We choose NOAA AR 11158 as the target due to its complex magnetic structure, rapid evolution and abundant activities. The AR produced the first X-class flare in Solar Cycle 24, and many observational studies have concentrated on it (Schrijver et al. 2011; Tan et al. 2012; Maurya et al. 2012; Beaugard et al. 2012; Gosain 2012; Dolla et al. 2012; Alvarado-Gómez et al. 2012; Petrie 2012; Jing et al. 2012).

The data and the evolution of the non-potentiality in the AR are briefly described in Section 2. The confirmation of earlier results is presented in Section 3. Section 4 reports new results on the changes and evolutions of the non-potentiality during four major flares of the AR. Section 5 summarizes the results and discusses the possible reasons for the changes and evolutions.

2 OBSERVATION

The vector magnetograms we used were observed by using the *SDO*/HMI from 2011 February 12 to 16 with a spatial resolution of $\sim 1''$ and a cadence of 12-min, and then reduced by using the HMI science data processing pipeline tool¹. The Stokes parameters I , Q , U and V from the FeI 6173 Å spectral line were calculated by using the Very Fast Inversion of the Stokes Vector (VFISV) algorithm (Borrero et al. 2011). Afterwards, the ‘minimum energy’ (Metcalf 1994; Metcalf et al. 2006; Leka et al. 2009) solution was used to resolve the 180-degree ambiguity and then the images were remapped with a Lambert cylindrical equal area projection. Finally, the magnetic field vector in each pixel of the data set was transformed to a three-dimensional rectangular coordinate system with a vertical component z and two horizontal components x and y .

It is clear that the accuracy of calculated non-potential parameters depends on the reliability of vector magnetograms. For the strong magnetic field of AR 11158, we could use a high threshold to filter noise. In this work, only the pixels with a vector magnetic field (B) stronger than 300 G were considered. Because the work is about the variation of observed values rather than their absolute value, setting a threshold would only cause a minor effect. The simultaneous ultraviolet 1600 Å images taken by the Atmospheric Imaging Assembly (AIA; Lemen et al. 2012) on *SDO* were also employed to investigate the flare ribbons.

AR 11158 was a complex quadrupolar system that produced one X-class, five M-class and 56 C-class flares from 2011 February 9 to 21. The data set in our work covered the entire quick growth phase and four major flares ($\geq M1.0$, see Table 1). In the growth phase, numerous magnetic fluxes emerged and 10 key EFRs were identified in the vector magnetograms with a $205'' \times 125''$ field of view (FOV) as shown in Figure 1. The EFRs were identified by the emerging time, the motion, the magnetic flux of the opposite polarities and the appearance of arches on AIA extreme ultraviolet images.

Table 1 Four Major Flares ($\geq M1.0$) of NOAA AR 11158 from 2011 February 12 to 16

Date	Start time (UT)	Peak time (UT)	End time (UT)	X-ray class
Feb 13	17:28	17:38	17:47	M6.6
Feb 14	17:20	17:26	17:32	M2.2
Feb 15	01:44	01:56	02:06	X2.2
Feb 16	14:19	14:25	14:29	M1.6

¹ <http://jsoc.stanford.edu/jsocwiki/ClickHereForDataRelease>

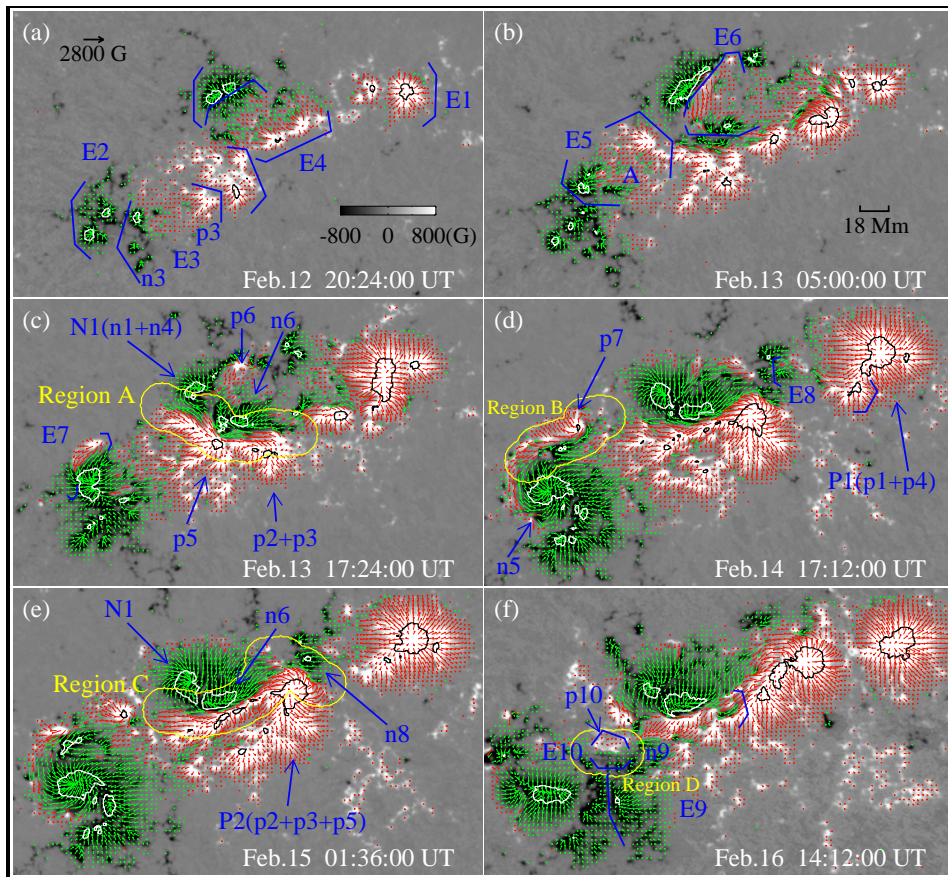


Fig. 1 Overview of vector magnetograms in NOAA AR 11158 from 2011 February 12 to 16. The vertical magnetic component is presented by black-and-white patches and isogauss contours with levels 1500 G (black) and -1500 G (white). Green and red arrows denote the horizontal magnetic component. The field of view (FOV) in each panel is about $205'' \times 125''$. E1–E6 in (a) and (b) indicate six major EFRs and E7–E10 in (c), (d) and (f) show four other smaller ones. Letters ‘p’ and ‘n’ with numbers indicate the positive and negative polarities that come from corresponding EFRs, respectively. (c)–(f) show the vector magnetic fields just before the onset times of the four major flares (M6.6, M2.2, X2.2 and M1.6), respectively. The yellow contours in the four panels outline regions A, B, C and D (see Sect. 4).

The first EFR (E1) started emerging when the AR was near the east limb of the Sun at about 23:00 UT on February 9. The second one (E2) followed it and came out from the southeast of E1 (see Fig. 1a). E3 and E4 appeared one after another in the middle of February 12 and contributed $\sim 1 \times 10^{21}$ Mx and $\sim 3 \times 10^{21}$ Mx to the total unsigned flux of the AR, respectively. The positive and the negative polarities of E3 (p3 and n3, respectively hereafter) separated at an average speed of ~ 0.7 km s^{-1} . Finally, they merged with the two polarities of E2.

The crucial E5 and E6 sprang up almost simultaneously and doubled the unsigned flux of the AR on February 13. Meanwhile, a δ -sunspot that contained p5, n6 and their predecessors was formed. As can be seen in Figure 1b, the vector magnetic field is obviously horizontal in area A. It indicates that E5 was emerging in the area with a similar direction as E2 and E3, and brought $\sim 5 \times 10^{21}$ Mx flux

to the AR at 17:24 UT on February 13. The two polarities of E5 separated at a speed of $\sim 1.5 \text{ km s}^{-1}$. We noted that the emergence of E6 had a similar location but an opposite direction compared to the previous E4. The opposite direction led to a magnetic cancellation between p6 and N1 (the combination of n1 and n4) and eventually caused p6 to vanish. Furthermore, n6 met the fast moving p5 and soon the first major flare of the AR erupted (Fig. 1(c)).

E7 was a smaller but important EFR that came out from a location close to n5. On February 14, when p7 was accelerated and encountered negative polarities from area A, the second major flare of the AR began (Fig. 1(d)). Towards the northwest of the AR, another small EFR (E8) simultaneously emerged from an area near P1 (the combination of p1 and p4). The n8 encountered P2 (the combination of p2, p3 and p5) on February 15 and it might have triggered the biggest flare of the AR, which was the first X-class flare of Solar Cycle 24. The last major flare of our data set erupted on February 16, when E9 and E10 were emerging (see Fig. 1(f)). The cancellation between p10 and n9 might have caused this flare.

3 CONFIRMATION OF EARLIER RESULTS

Through the excellent HMI vector magnetograms, we confirmed many earlier results about the non-potentiality in the complex AR 11158.

As mentioned above, the collision and cancellation between opposite polarities of the different EFRs play an important role in the occurrence of the flares of the AR, which is in line with a recent study about another complex AR (Yan et al. 2012). Furthermore, as former studies showed (Wang et al. 1994b; Leka et al. 1996), EFRs brought significant vertical electric currents and other non-potential parameters to the AR. The first five EFRs (E1–E5) emerged with approximately equal positive and negative current helicity. When E6 rapidly sprang up in the opposite direction to its predecessor, the balance was disrupted. It is noted that N1 changed its sign from negative to positive (Fig. 2(a) and (b)). After the emergence of E5 and E6, N1, n6 and p5 were concentrated in three new current cores with different signs (Fig. 2(c)). As we can see in Figure 2(d), a strong negative shear belt ($\leq -80^\circ$) outlined the PIL. The increase of this belt during the flare was also found in our work as well as previous works which used slightly different definitions of angle (Wang et al. 1994a, 2002; Sun et al. 2012). The box in Figure 2(d) indicated an area with opposite angular shear, which will be discussed in Section 5.

As illustrated by Figure 3, the evolutions of the magnetic flux and non-potential parameters were not uniform. Park et al. (2008) classified the process of magnetic helicity accumulation that occurs before a flare into two phases, a monotonically increasing phase and a relatively constant phase. The two phases (I and II) that occur before the X-class flare were confirmed in the evolution of AR 11158 and the AR changed to an undulating decrease phase (III) after the flare (Fig. 3(b)). As listed in Table 2, the growth of the AR was mainly in phases I and II. The unsigned flux, current and helicity had a fast and a slow increase in phases I and II, respectively. However, both the unsigned angular shear and total free energy had a sharp rise in the middle of phase I and continued a fast increase in phase II. The variations of the current, helicity, and free energy were declining in phase III, but the variations of the flux and angular shear were still rising. The major flares happened only when the flux and non-potentiality of the AR reached a high level. During and after phase III, the frequency of occurrence and intensity of the major flare decreased, while the flux was still relatively high. It confirms that the non-potentiality, instead of the magnetic flux, has a stronger connection with the flare. The total positive and negative fluxes maintained a balance during phase II while the positive and negative currents had a minor imbalance through all the three phases. The negative helicity peaked when the M2.2 flare broke out and dropped immediately after the X2.2 flare erupted. On average, the negative shear was 2.3 times as large as the positive shear during the five days.

Figure 4 shows difference maps of the B_z , B_h , h_c and ρ_{free} for the X2.2 flare. The flare ribbons appeared as a double-J configuration laid astride with respect to the PIL. Besides of smaller enhanced

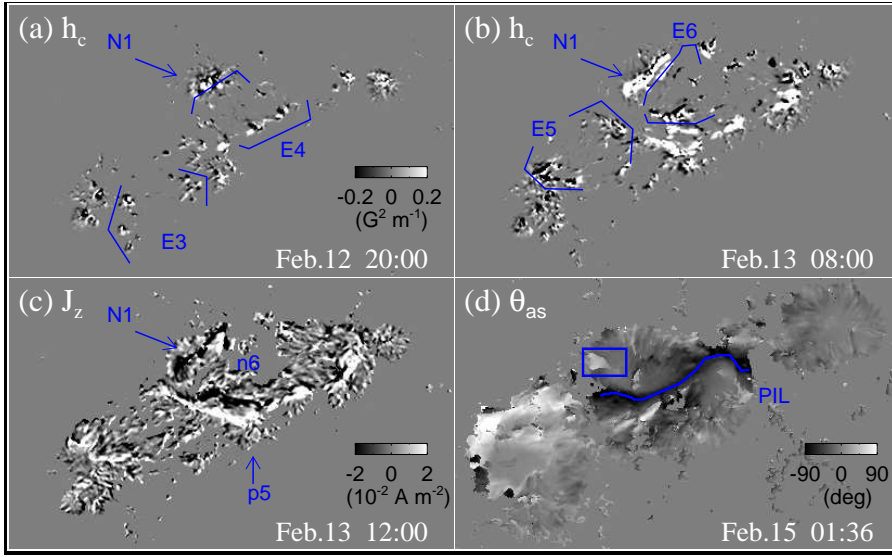


Fig. 2 Maps of fractional current helicity (h_c), vertical current (J_z) and angular shear (θ_{as}). The FOV and EFRs are the same as in Fig. 1. The curve in (d) shows the magnetic PIL and the box indicates an area with an opposite sign for θ_{as} which is discussed in Section 5.

Table 2 Three phases of evolution of the non-potentiality of AR11158 from 2011 February 12 to 16. The first line of each phase is the average rate of daily change and the second line gives the percent of the change in the corresponding phase.

Phase	Start Time End Time (UT)	Flux (10^{22} Mx d $^{-1}$)	Current (10^{13} A d $^{-1}$)	Helicity (10^{16} cm G 2 d $^{-1}$)	Angular Shear (10^{20} deg cm 2 d $^{-1}$)	Free Energy (10^{23} erg cm $^{-1}$ d $^{-1}$)
I	Feb 12 14:00 Feb 13 17:28	1.03 (47.8%)	2.78 (66.8%)	2.10 (64.0%)	5.34 (46.0%)	2.67 (50.3%)
II	Feb 13 17:28 Feb 15 01:44	0.560 (26.1%)	0.559 (15.7%)	0.503 (17.8%)	3.25 (32.6%)	1.90 (41.6%)
III	Feb 15 01:44 Feb 16 23:48	0.128 (8.53%)	-0.226 (-9.07%)	-0.241 (-12.2%)	0.658 (9.44%)	-0.673 (-21.1%)

and weakened areas, there are two bigger enhanced areas (B and C) in the difference map of B_z . Area B was due to the emergence of magnetic flux, while area C came from the fast moving P2 (Fig. 4(a)). The fast changes of B_h around PIL during the flare are confirmed in the present work as well as previous works (Fig. 4(b)). The B_h of the X2.2 flare had significant enhancement in the junction of these two J-shaped structures where Wang et al. (2012) found a 30% increase during the flare. The B_h of all four flares appeared to have an obvious enhancement on the flare ribbons and was reduced in the outskirts, which is consistent with a previous result (Wang et al. 2009). The biggest enhanced areas in h_c were in the same location as the negative polarity n6. The greatest area that receded in this parameter was cospatial with the negative polarity N1 (Fig. 4(c)). The ρ_{free} also had a significant enhancement in the junction of these two Js (Fig. 4(d)).

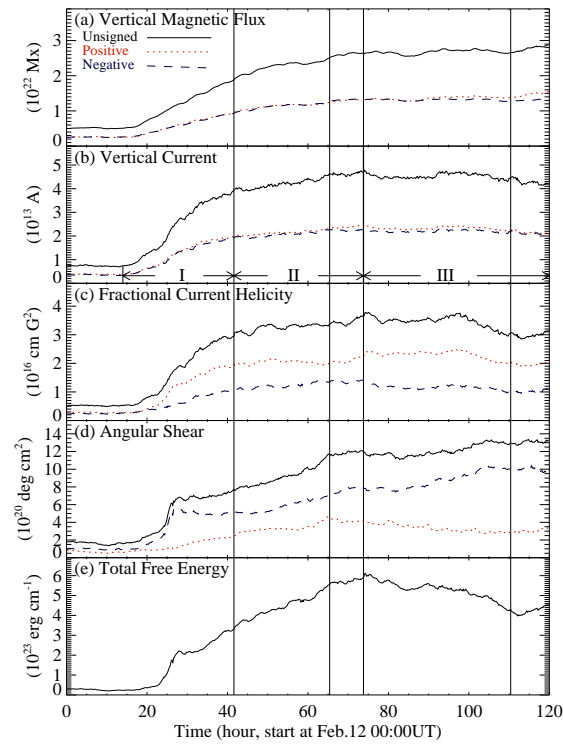


Fig. 3 Evolution of magnetic flux and four non-potential parameters of AR 11158 in five days. (a) is the variation of total unsigned, positive and negative magnetic flux. The four long vertical lines in each panel indicate the onset times of the four flares. (b)–(d) have the same line styles as (a) but for the variations of vertical currents, current helicities and angular shears. (e) is the variation of total free energy. (b) also gives the three phases of the evolution (see Table 2).

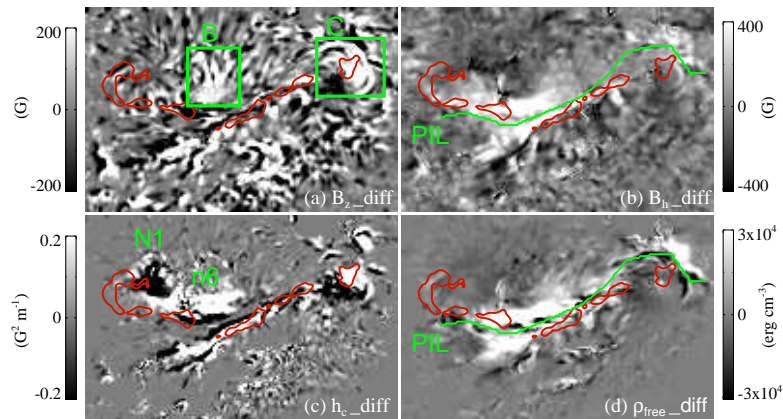


Fig. 4 Difference maps of vertical magnetic component (B_z), horizontal magnetic component (B_h), h_c and free energy density (ρ_{free}) for the X2.2 flare at 01:36 and 02:24 UT on February 15. The FOV of each panel is about $80'' \times 53''$. The red contours denote flare ribbons at 01:47 UT and the green curves show the PIL. The boxes in (a) indicate areas with enhanced B_z .

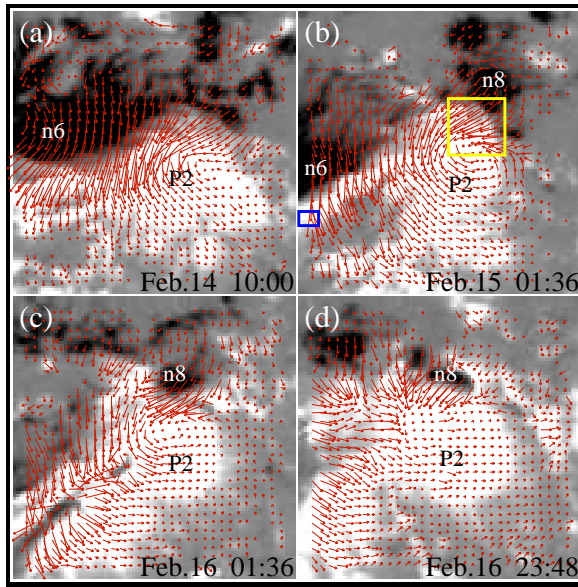


Fig. 5 Vortex of source field (B_s) of P2. The B_s is represented by arrows with length proportional to the relative field strength. The B_z is represented by gray-scale patches. The FOV of each panel is about $25'' \times 25''$. The blue and yellow boxes in (b) are the as same as those in Fig. 6 to show the locations.

4 NEW RESULTS

The B_s and B_z of P2 are mapped in Figure 5 to give an example of vortices of the B_s . The B_s is represented by arrows with length proportional to the relative field strength and the B_z is represented by gray-scale patches. The FOV of each panel is about $25'' \times 25''$. The blue and yellow boxes in Figure 5(b) are the same as those in Figure 6 to show the locations of two small areas that will be described below. By definition, the strength of B_s is proportional to the square root of ρ_{free} . Therefore, its distribution and variation are similar to the free energy. However, the direction of B_s has additional information about the non-potentiality. Around the PIL of the AR, the strength of B_s was stronger and the direction was from negative to positive magnetic polarities (Fig. 5(a)). Then a counterclockwise vortex appeared at the west end of the flare ribbons about 15 h before the X2.2 flare (Fig. 5(b)). As Figure 5(c) shows, the vortex was still evident one day after the flare when P2 was rotating around its center and canceling with n8. The vortex disappeared the next day, as did n8 (Fig. 5(d)). In the meantime, the unsigned current helicity decreased $\sim 4.1 \times 10^{15} \text{ cm G}^2$ (34%) in the area.

The B_s of N1 and n5 also had vortices. The B_s of N1 formed a clockwise vortex about 9 h before the first major flare and the vortex developed over the next two days. The east end of the M6.6 flare ribbons overlapped with this vortex, while the X2.2 flare ribbons partly overlapped. A counterclockwise vortex around n5 formed in late February 13, then became enhanced about 13 h before the M2.2 flare, and finally vanished on February 16. Simultaneously, n5 rotated at least 180° about its center.

Figure 6 shows two areas that had evident changes of the direction of B_h (e.g. azimuth). Green and red arrows denote the B_h . The B_z is represented by black-and-white patches and isogauss contours with levels 1500 G (black) and -1500 G (white). The FOV of each panel is about $12.5'' \times 12.5''$. The blue arrows indicate the average azimuths in the boxes. The northwest part of P2 started a di-

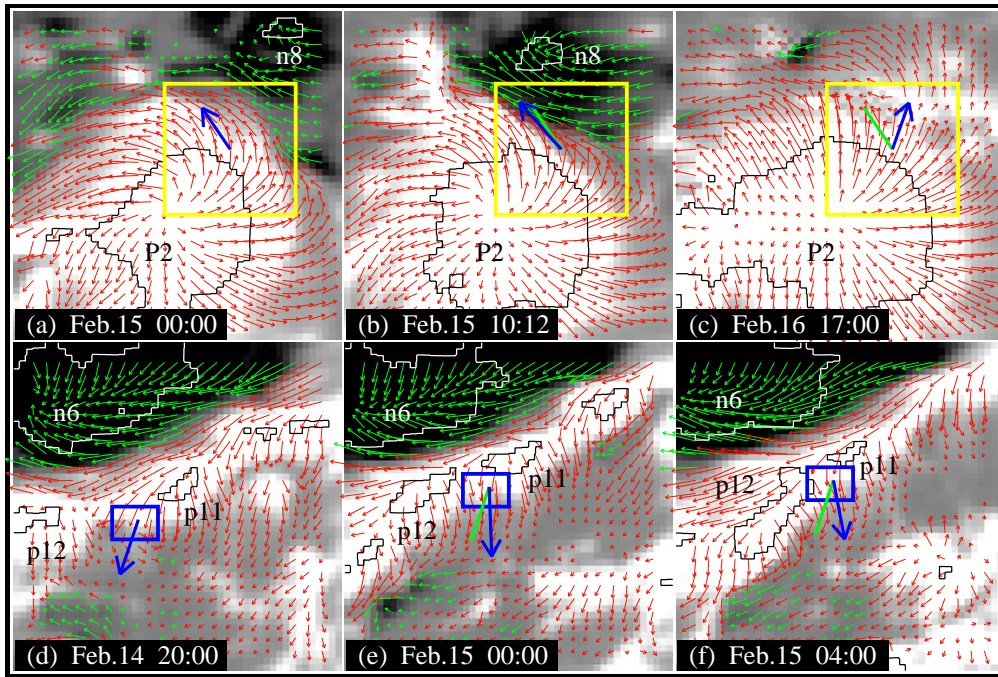


Fig. 6 Changes of the direction of B_h (e.g. azimuth) in two small areas. The FOV of each panel is about $12.5'' \times 12.5''$. The set of vector magnetograms is similar to that in Fig. 1. The blue and yellow boxes are the as same as those in Fig. 5. The blue arrows indicate the average azimuths in the boxes.

rect interaction with the opposite polarity n8 before the X-class flare (see Fig. 6(a) and the yellow box in Fig. 5(b)). After the flare, the two polarities canceled with each other even faster than before the flare. As illustrated by the arrows, the average azimuth inside the yellow box rotated counter-clockwise $\sim 7.5^\circ$ and turned more parallel to the PIL. The cancellation continued even 10 h after the flare (Fig. 6(b)). About $\sim 3.9 \times 10^{20}$ Mx of negative magnetic flux was canceled in the area from 00:00 UT on February 15 to 17:00 UT on February 16. Almost all negative magnetic flux in the area (96%) was canceled. Meanwhile, the rotation of B_h became clockwise, which means the vector magnetic field of P2 started to have more potential. After n8 disappeared by the cancellation, the average azimuth had a change of 54° compared to that of the preflare. The rate of change was about 1.3° h^{-1} .

In the neighborhood southeast of P2, a complex area also had an evident change of the average azimuth (see Fig. 6(d) and the blue box in Fig. 5(b)). A strong PIL crossed the area and the negative polarities of E9 passed the area (also see Fig. 1(f) and Fig. 2(d)). In the meantime, several positive polarities merged there. The change of average azimuth was remarkable in the blue box between the two positive polarities that were merging (p11 and p12). The change of average azimuth inside the box during 8 h was about 29° with a rate of 3.6° h^{-1} (Fig. 6(f)).

Four regions are outlined by the yellow contours on panels (c)–(f) in Figure 1 to investigate the change of the non-potentiality for the four flare events. Each pixel in those regions has a distance less than 15 Mm from the PIL (Schrijver 2007). The main parts of the initial brightening in 1600 \AA showing the flare ribbons are located in these regions. These four selected regions are denoted as regions A, B, C and D, respectively. The variations of B_z and the four non-potential parameters

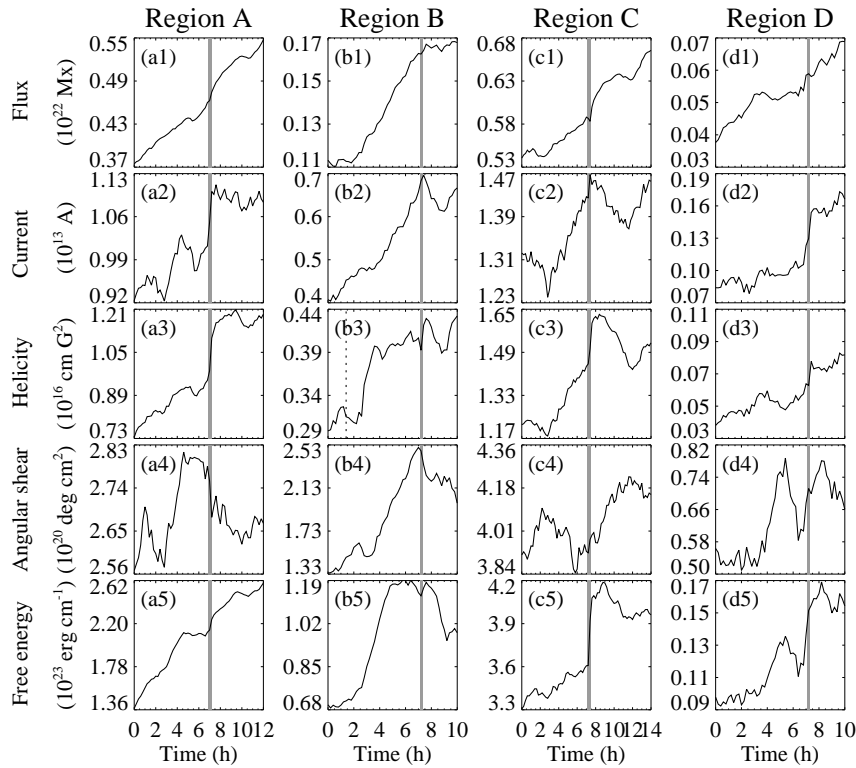


Fig. 7 Variations of the vertical magnetic flux and the four non-potential parameters that occur in processes of the flares. *Rows*: Unsigned vertical magnetic flux, unsigned vertical current, unsigned fractional current helicity, unsigned angular shear and total free energy; *Columns*: four regions for the flares as shown in Fig. 1. Abscissas are times that start at Feb. 13 10:36, Feb. 14 10:12, Feb. 14 18:36 and Feb. 16 07:36 UT, respectively. The gray shadow in each panel indicates the duration of the corresponding flare. The dotted line in (b3) shows the time when the movement of p7 and the rotation of n5 both accelerated.

during the occurrence of the four flares in these initial brightening regions are detailed in Figure 7. Abscissas are times that start at Feb. 13 10:36, Feb. 14 10:12, Feb. 14 18:36 and Feb. 16 07:36 UT, respectively. The gray shadow in each panel indicates the duration of the corresponding flare.

Most of the parameters increase before the flares and decrease after them. We found that the unsigned magnetic flux in regions A and C continued increasing and reached their peaks 2–3 h after the flares, but the other two did not show this conspicuous change. These variations of regions A and C are more significant if we enlarge the regions to include the entire P2 and N1. The unsigned current helicity had a fast and significant increase in each region and then slowly reverted. The dotted line in panel b3 of Figure 7 indicates the time when p7 began its fast proper motion and about one hour later the unsigned helicity started to rapidly increase. The unsigned current had similar but temperate increases except in region D. The unsigned angular shear rose before the first two flares and started declining immediately before the onset of these flares. The total free energy in region C had a rapid increase of more than 10% during the X2.2 flare while other regions had smaller increases. The reason for these changes and other issues will be discussed in the next section.

5 DISCUSSION AND SUMMARY

Benefitting from state-of-the-art vector magnetograms from *SDO/HMI*, we studied the long-term evolution of AR 11158 and the short-term change of the non-potentiality during four major flares in the AR. We confirm that the non-potentiality, instead of the magnetic flux, had a closer connection with the flare. The EFRs were important for the non-potentiality and flares of the AR because they increased the non-potentiality and brought the crucial opposite sign of non-potentiality to the AR. AR 11158 was formed by contributions from 10 key EFRs that simultaneously occurred or quickly subsided within five days. The interaction between opposite polarities of the EFRs may be a likely cause of some major flares. Some crucial EFRs could impact the imbalances of the whole AR. The evolutions of non-potential parameters were quickly increasing as major EFRs were emerging in phase I. The major flares happened only when the flux and non-potentiality of the AR reached a high level. The current, helicity, and free energy declined in phase III, but the flux still rose. The rapid increase of ρ_{free} and h_c around PIL during the flare was found in our work, which is the same as what was found in previous studies. We also identified a decrease at the outskirts of the flare's initial brightening regions for the two non-potential parameters, as well as in earlier studies.

Sunspot n5 had fast and significant rotation before the M2.2 flare and Jiang et al. (2012) found that sunspot P2 had a rapid rotation before the X2.2 flare. The relationship between the sunspot rotation and the major flare has been discussed in previous works (Zhang et al. 2007; Yan et al. 2008). The B_s vortex in our work directly displayed the deflection of B_h . The evolution of the vortices were delayed by a few hours with respect to the rapid rotations of the sunspots. This might suggest that the sunspot rotation leads to an increase in the non-potentiality of the AR.

Liu et al. (2012) used the nonlinear force-free field (NLFFF) to reconstruct the three-dimensional coronal magnetic field and explained the increase of B_h with the tether-cutting model (Moore et al. 2001) for the M6.6 flare event of AR 11158. Sun et al. (2012) gave a similar result for the X2.2 flare of the AR. According to the model and the NLFFF reconstruction, the coronal magnetic field collapses after the flare. The vector magnetic field of the photosphere becomes more inclined, i.e. B_h increases and B_z decreases. However, we found that the vertical magnetic flux increased instead decreased in the three biggest flares of the AR. After the M6.6 and the X2.2 flares, the unsigned flux increased faster than the pre-flare stage (see Figs. 7 a1, c1). This suggests that there were magnetic emergences in regions A and C, and they were accelerated. Therefore the coronal magnetic collapse is just one reason for the B_h enhancement, and the magnetic flux emerging onto the photosphere is another one. The accelerated emergences may be linked to the flares, but the reason why the emergences of regions A and C are accelerated but the other two are not is not yet clear. Our future work will concentrate on this aspect.

Another difference between regions A and C and regions B and D is in the unsigned helicity. All four regions had a fast and significant increase during the flares and then returned to a minimum. However, regions A and C had a longer recovery time (3–4 h) than regions B and D (< 2 h). It may be due to regions A and C being bigger and they covered the δ -sunspot of the AR which contains a complex and pivotal magnetic structure. When the bigger, complex and pivotal magnetic structure changed in a major flare, it would take more time to restore the field to the previous state.

The decrease caused the decline in the unsigned angular shear of regions A and B during the flares. The unsigned shear of the entire AR had a similar evolution to the unsigned flux, especially in phases II and III. The change of unsigned shear of the four regions did not agree with that of the unsigned flux, even if we enlarge the regions to include the entire polarities. The reason may be that the regions are not independent of the AR in terms of being non-potential, or there is an unknown mechanism that makes these regions special.

An interesting correlation is found related to the X2.2 flare of the AR. The small area indicated by a box in the θ_{as} map of Figure 2 has an opposite sign in the angular shear and it is basically co-spatial with the source region of the sunquake event which has been investigated by Kosovichev (2011)

and Zharkov et al. (2011). The area enlarged before the X2.2 flare and shrank after it. Afterwards, a magnetic structure split from a location next to the area on February 16. It may suggest that this area has a different magnetic topology compared to its vicinity and becomes the key to the outburst event. We will do more research to find the reason for the correlation.

The main results of this work are summarized as follows:

- (1) The vortex in the source field directly displayed the deflection of B_h . The deflection corresponded to the fast rotating sunspots, but had a time delay, which suggests that sunspot rotation leads to an increase of the non-potentiality.
- (2) Two areas that had evident changes in the azimuth of the vector magnetic field were found near the PIL. The change rates of the azimuth were about 1.3° h^{-1} and 3.6° h^{-1} , respectively.
- (3) Rapid and prominent increases were found in the variations of unsigned helicity during all four flares in their initial brightening regions. The recovery of the increases took 3–4 h for the two bigger flares, but only took less than 2 h for the two other smaller flares. This may be due to regions A and C being covered by the δ -sunspot of the AR which contains a bigger, complex and pivotal magnetic structure.

More samples of ARs with high quality vector magnetograms are needed to detect the precise role of the non-potentiality.

Acknowledgements We thank Prof. Jingxiu Wang for his valuable suggestions. The data have been used by courtesy of NASA/SDO and the HMI science team. SDO is a mission for NASA's Living With a Star program. The work is supported by the National Basic Research Program of China (973 program, Grant No. 2011CB811403), the National Natural Science Foundation of China (Grant Nos. 11025315, 10921303, 10973019, 11003024, 40890161, 11203037 and 41074123) and the CAS Project KJCX2-EW-T07.

References

- Abramenko, V. I., Wang, T., & Yurchishin, V. B. 1996, *Sol. Phys.*, 168, 75
 Alvarado-Gómez, J. D., Buitrago-Casas, J. C., Martínez-Oliveros, J. C., et al. 2012, *Sol. Phys.*, 131
 Bao, S., & Zhang, H. 1998, *ApJ*, 496, L43
 Beauregard, L., Verma, M., & Denker, C. 2012, *Astronomische Nachrichten*, 333, 125
 Borrero, J. M., Tomczyk, S., Kubo, M., et al. 2011, *Sol. Phys.*, 273, 267
 Deng, Y., Wang, J., Yan, Y., & Zhang, J. 2001, *Sol. Phys.*, 204, 11
 Dolla, L., Marqué, C., Seaton, D. B., et al. 2012, *ApJ*, 749, L16
 Dun, J., Kurokawa, H., Ishii, T. T., Liu, Y., & Zhang, H. 2007, *ApJ*, 657, 577
 Gary, G. A., Moore, R. L., Hagyard, M. J., & Haisch, B. M. 1987, *ApJ*, 314, 782
 Gosain, S. 2012, *ApJ*, 749, 85
 Hagyard, M., Low, B. C., & Tandberg-Hanssen, E. 1981, *Sol. Phys.*, 73, 257
 Hagyard, M. J., Teuber, D., West, E. A., & Smith, J. B. 1984, *Sol. Phys.*, 91, 115
 Jiang, Y., Zheng, R., Yang, J., et al. 2012, *ApJ*, 744, 50
 Jing, J., Park, S.-H., Liu, C., et al. 2012, *ApJ*, 752, L9
 Kopp, G., Lawrence, G., & Rottman, G. 2005, *Sol. Phys.*, 230, 129
 Kosovichev, A. G. 2011, *ApJ*, 734, L15
 Leka, K. D., Barnes, G., Crouch, A. D., et al. 2009, *Sol. Phys.*, 260, 83
 Leka, K. D., Canfield, R. C., McClymont, A. N., & van Driel-Gesztelyi, L. 1996, *ApJ*, 462, 547
 Lemen, J. R., Title, A. M., Akin, D. J., et al. 2012, *Sol. Phys.*, 275, 17
 Liu, C., Deng, N., Liu, R., et al. 2012, *ApJ*, 745, L4
 Lu, Y., Wang, J., & Wang, H. 1993, *Sol. Phys.*, 148, 119

- Maurya, R. A., Vemareddy, P., & Ambastha, A. 2012, *ApJ*, 747, 134
- Metcalf, T. R. 1994, *Sol. Phys.*, 155, 235
- Metcalf, T. R., Leka, K. D., Barnes, G., et al. 2006, *Sol. Phys.*, 237, 267
- Moon, Y.-J., Yun, H. S., Choi, G., Park, Y. D., & Mickey, D. L. 2000, *Journal of Korean Astronomical Society*, 33, 47
- Moore, R. L., Sterling, A. C., Hudson, H. S., & Lemen, J. R. 2001, *ApJ*, 552, 833
- Park, S.-H., Chae, J., Jing, J., Tan, C., & Wang, H. 2010, *ApJ*, 720, 1102
- Park, S.-H., Lee, J., Choe, G. S., et al. 2008, *ApJ*, 686, 1397
- Pesnell, W. D., Thompson, B. J., & Chamberlin, P. C. 2012, *Sol. Phys.*, 275, 3
- Petrie, G. J. D. 2012, *Sol. Phys.*, 183
- Sakurai, T. 1989, *Space Sci. Rev.*, 51, 11
- Schou, J., Scherrer, P. H., Bush, R. I., et al. 2012, *Sol. Phys.*, 275, 229
- Schrijver, C. J. 2007, *ApJ*, 655, L117
- Schrijver, C. J., Aulanier, G., Title, A. M., Pariat, E., & Delannée, C. 2011, *ApJ*, 738, 167
- Schrijver, C. J., De Rosa, M. L., Metcalf, T., et al. 2008, *ApJ*, 675, 1637
- Schrijver, C. J., De Rosa, M. L., Title, A. M., & Metcalf, T. R. 2005, *ApJ*, 628, 501
- Sun, X., Hoeksema, J. T., Liu, Y., et al. 2012, *ApJ*, 748, 77
- Tan, B., Yan, Y., Tan, C., Sych, R., & Gao, G. 2012, *ApJ*, 744, 166
- Wang, H., Ewell, M. W., Jr., Zirin, H., & Ai, G. 1994a, *ApJ*, 424, 436
- Wang, H., Spirock, T. J., Qiu, J., et al. 2002, *ApJ*, 576, 497
- Wang, J. 1999, *Fund. Cosmic Phys.*, 20, 251
- Wang, J., Shi, Z., Wang, H., & Lue, Y. 1996, *ApJ*, 456, 861
- Wang, J., Zhao, M., & Zhou, G. 2009, *ApJ*, 690, 862
- Wang, J., Zhou, G., & Zhang, J. 2004, *ApJ*, 615, 1021
- Wang, S., Liu, C., Liu, R., et al. 2012, *ApJ*, 745, L17
- Wang, T., Xu, A., & Zhang, H. 1994b, *Sol. Phys.*, 155, 99
- Yan, X.-L., Qu, Z.-Q., & Kong, D.-F. 2008, *MNRAS*, 391, 1887
- Yan, X. L., Qu, Z. Q., & Kong, D. F. 2012, *AJ*, 143, 56
- Zhang, J., Li, L., & Song, Q. 2007, *ApJ*, 662, L35
- Zharkov, S., Green, L. M., Matthews, S. A., & Zharkova, V. V. 2011, *ApJ*, 741, L35